DTU Library

Engineering nanoscale hypersonic phonon transport

Florez, O.; Arregui, G.; Albrechtsen, M.; Ng, R. C.; Gomis-Bresco, J.; Stobbe, S.; Sotomayor-Torres, C. M.; García, P. D.

Check for updates

Engineering nanoscale hypersonic phonon transport

O. Florez [1,2 ✉], G. Arregui[1], M. Albrechtsen [3], R. C. Ng [1], J. Gomis-Bresco[1], S. Stobbe [3,4], C. M. Sotomayor-Torres [1,5] and P. D. García [1 ✉]

Controlling vibrations in solids is crucial to tailor their elastic properties and interaction with light. Thermal vibrations represent a source of noise and dephasing for many physical processes at the quantum level. One strategy to avoid these vibrations is to structure a solid such that it possesses a phononic stop band, that is, a frequency range over which there are no available elastic waves. Here we demonstrate the complete absence of thermal vibrations in a nanostructured silicon membrane at room temperature over a broad spectral window, with a 5.3-GHz-wide bandgap centred at 8.4 GHz. By constructing a line-defect waveguide, we directly measure gigahertz guided modes without any external excitation using Brillouin light scattering spectroscopy. Our experimental results show that the shamrock crystal geometry can be used as an efficient platform for phonon manipulation with possible applications in optomechanics and signal processing transduction.

Nanostructured materials offer the possibility to manipulate the mechanical vibrations of a solid over a specified spectral bandwidth. This in turn enables the control of light–matter interactions in the visible and near-infrared regimes for optomechanical applications ranging from high-resolution accelerometers[1] to mass and force sensors[2,3], in addition to providing fundamental insights into phenomena such as quantum ground-state cooling[4,5]. By periodically distributing the mass within a system, it is possible to engineer its mechanical modes[6,7] and open frequency windows over which the destructive interference of scattered waves forbids any phonon propagation[8,9]. This approach enables engineering of the thermal conductance of the structure[10] and allows for the routing of phonons at the mesoscale[11,12]. Although full-gap gigahertz phononic crystals are widely used in optomechanical systems to create phononic shields[13], waveguides[14,15] and cavities[16,17], clear and direct experimental evidence of a complete omnidirectional phononic bandgap at hypersonic (GHz) frequencies is still lacking. Existing experimental work is generally limited to megahertz frequencies up to the 1 GHz band, using piezoelectric materials to drive the system[18–22], requiring varying interdigitated electrodes to probe different frequencies and propagation directions. In the gigahertz regime, only partial and narrow mechanical bandgaps (with up to 8% gap-to-midgap ratio) have been shown using assembled platforms such as colloidal crystals[23] or two-dimensional phononic crystal membranes[24]. Furthermore, the control and guiding of elastic waves at gigahertz frequencies has been difficult to achieve or measure, relying on complex optomechanical systems[14,15] or nonlinear stimulated phenomena[25].

Here we report direct experimental evidence of a wide full phononic gap with a central frequency at 8.4 GHz and a spectral width of 5.3 GHz (a gap-to-midgap ratio of 64%) in a free-standing patterned silicon membrane phononic crystal. Additionally, we create a line-defect waveguide with the same geometry in which we directly measure two guided modes at 5.7 GHz and 7.1 GHz within the bandgap at room temperature. We demonstrate the passive spectral tunability of the mechanical gap as a function of the geometric parameters of the crystal, with a spectral shift spanning the range from approximately 4 GHz to 11.5 GHz, which subsequently also enables spectral tunability of the guided modes.

Shamrock phononic crystal design

All the structures measured here are fabricated on a silicon-on-insulator (SOI) platform, which readily enables integration with electronic and photonic circuits. Figure 1a shows a scanning electron micrograph (SEM) of the fabricated pattern composed of a triangular array of 'shamrocks'[26,27], formed by three tangential circles with nominal parameters of thickness $t = 220$ nm, period $a = 330$ nm, and radius $r = 0.22a$, as detailed in the inset of Fig. 1a and Supplementary Fig. 1. We calculate the phononic dispersion relation of the structure by solving the full three-dimensional elastic wave equation using finite-element simulations performed with COMSOL Multiphysics[28].

Figure 1b plots the symmetric (blue) and asymmetric (red) acoustic modes with respect to the mid-plane of the silicon slab, calculated over the entire first Brillouin zone of the crystal. We use the geometrical parameters extracted from SEM images to more accurately simulate the real shape of the fabricated crystal (Supplementary Fig. 4). We also take into account the anisotropy of the silicon stiffness tensor and its particular orientation with respect to the fabricated samples, as detailed in Fig. 1a. Owing to this mechanical anisotropy, the irreducible Brillouin zone is determined by the first quarter of the hexagon highlighted on the bottom part of Fig. 1b. A full mechanical gap opens between the sixth and seventh bands, from 6.7 GHz up to 11.4 GHz (gap-to-midgap ratio of 52%), which results in the complete depletion of the phonon density of states over this frequency range, as shown in Fig. 1c. The particular shape of the shamrock crystal, which comprises large masses connected by small necks, enables a distribution of the mass within the unit cell that results in this broad mechanical gap. A direct link exists between the spectral width of the gap and the

[1]Catalan Institute of Nanoscience and Nanotechnology (ICN2), CSIC and BIST, Campus UAB, Barcelona, Spain. [2]Departament de Física, Universitat Autònoma de Barcelona, Bellaterra, Spain. [3]Department of Electrical and Photonics Engineering, DTU Electro, Technical University of Denmark, Kgs. Lyngby, Denmark. [4]NanoPhoton – Center for Nanophotonics, Technical University of Denmark, Kgs. Lyngby, Denmark. [5]ICREA – Institució Catalana de Recerca i Estudis Avançats, Barcelona, Spain. ✉e-mail: omar.florez@icn2.cat; pd.garcia@csic.es
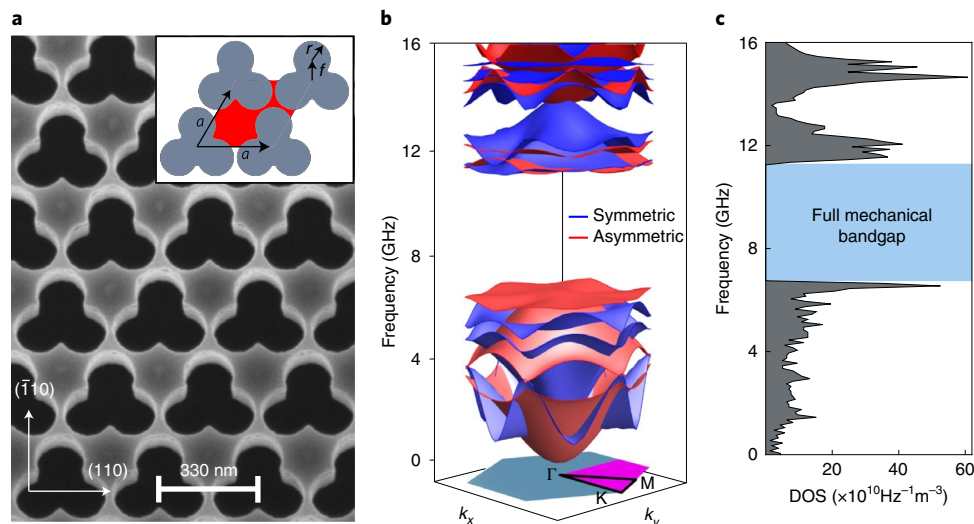
Fig. 1 | Shamrock phononic insulator. a, SEM (tilted-top view) of the fabricated structure on an SOI substrate with a thickness of $t = 220$ nm. Inset: schematic illustration of the geometrical parameters of the unit cell (highlighted in red) with lattice constant $a = 330$ nm, hole radius $r = 0.22a$, and the distance between the centre of the shamrock and the centre of each circle $f = 2r/\sqrt{3}$. **b**, Simulated three-dimensional phononic dispersion relation of the crystal over the first Brillouin zone. Blue and red curves indicate the symmetric and asymmetric modes with respect to the middle plane of the silicon slab at $t/2$. **c**, Calculated phononic density of states (DOS) of the structure. The light-blue region highlights the full mechanical gap spanning 6.7 GHz to 11.4 GHz.

narrow necks (shorter distance between shamrocks): a larger radius leads to narrower connected neck regions, which subsequently widens the gap[29].

Experimental reconstruction of the mechanical dispersion

We use Brillouin light scattering spectroscopy[30,31] to reconstruct the mechanical dispersion relation of the system. For simplicity, we probe the band structure along the ΓKMΓ path, highlighted at the bottom of Fig. 1b, as the edges of the gap do not change in frequency with respect to the irreducible Brillouin zone (Supplementary Section 2). When incident light with frequency ν_i and wavevector $\mathbf{k}_i$ reaches the surface of the sample with a certain angle, θ, as illustrated in Fig. 2a, part of it is linearly scattered while another small part is non-linearly scattered in all directions by thermally activated acoustic phonons. This scattering process occurs either by the photoelastic (PE)[32] or the moving-boundary[33] mechanism. The former is a volumetric effect caused by the acoustic modulation of the dielectric constant ϵ inside the material, while the latter is a surface effect induced by the movement of phonons that creates corrugation at the interface.

The interplay between these two effects can result in the enhancement[34] or the cancellation[35] of the scattering process. Given the high refractive-index contrast between silicon and the surrounding air, and the small volume of interaction, determined by the direction of the incident beam and the thickness of the suspended structure, the scattering process here is dominated by the moving-boundary mechanism. Our experiment collects the backscattered signal, $\mathbf{k}_s$, in Fig. 2a. For this configuration, the phase-matching condition for the mechanical wavevector $\mathbf{q}_\parallel$, which lies parallel to the surface, is determined by

$$q_\parallel = 2k_i \sin\theta = \frac{4\pi}{\lambda_i}\sin\theta, \qquad (1)$$

where $k_i = 2\pi/\lambda_i$. Therefore, it is possible to probe different mechanical wavevectors by changing the angle of incidence of light θ, illustrated in Fig. 2a, and subsequently map the dispersion relation of the acoustic phonons. All measurements were taken by focusing a green laser ($\lambda_i = 532$ nm) that is p-polarized with respect to the

sagittal plane formed by the angle θ (Supplementary Fig. 9). The scattered light that was analysed is also the p-polarized component. Although in-plane and out-of-plane elastic waves in bulk materials and membranes can be selectively detected using light polarization[36], elastic waves in phononic crystals are generally mixed. Therefore, we do not obtain different information by considering different polarizations of incident and analysed light.

Figure 2b plots the mechanical spectrum measured with incident angle $\theta = 32.5°$, which corresponds to the high-symmetry point K in reciprocal space. The central peak highlighted in green corresponds to the elastic (Rayleigh) scattered signal. Positive and negative frequencies correspond with anti-Stokes and Stokes contributions respectively, which are equally likely in a stochastic process such as spontaneous Brillouin scattering[32,37]. All the peaks observed in the spectrum correspond to vibrational modes of the system and their amplitudes depend on the scattering efficiency of each mode with the incident laser light[38], which is proportional to the displacement of the boundaries, as detailed in Supplementary Section 4. We obtain the phonon frequencies by fitting each of the observed peaks to Lorentzian line shapes and extracting the mean value between the resonant frequencies of the Stokes and anti-Stokes components. Figure 2c plots the mechanical dispersion relation along the ΓKMΓ path. The intensity colour scale represents the normalized coupling coefficients for the moving-boundary perturbation.

The sidewalls of our structures are angled at approximately 4° relative to vertical, which is taken into account in our band structure calculation, as shown in the inset of Fig. 2c. This breaks the up–down symmetry and the mechanical modes of the real structure therefore cannot be classified by their symmetry with respect to the mid-plane of the slab as done previously in Fig. 1b. For this reason, all bands in Fig. 2c are indicated with the same colour and only change in intensity to indicate the scattering efficiency of each mode and wavevector. We observe that this small correction to the vertical profile causes a displacement of about 1 GHz in the bands below the band-gap, which becomes evident upon comparing Figs. 2c and Fig. 1c. Additionally, the gap-to-midgap ratio increases from 52% in Fig. 1b,c to 64% in Fig. 2c. The black dots in Fig. 2c are the measured frequencies of the peaks as the incident angle is
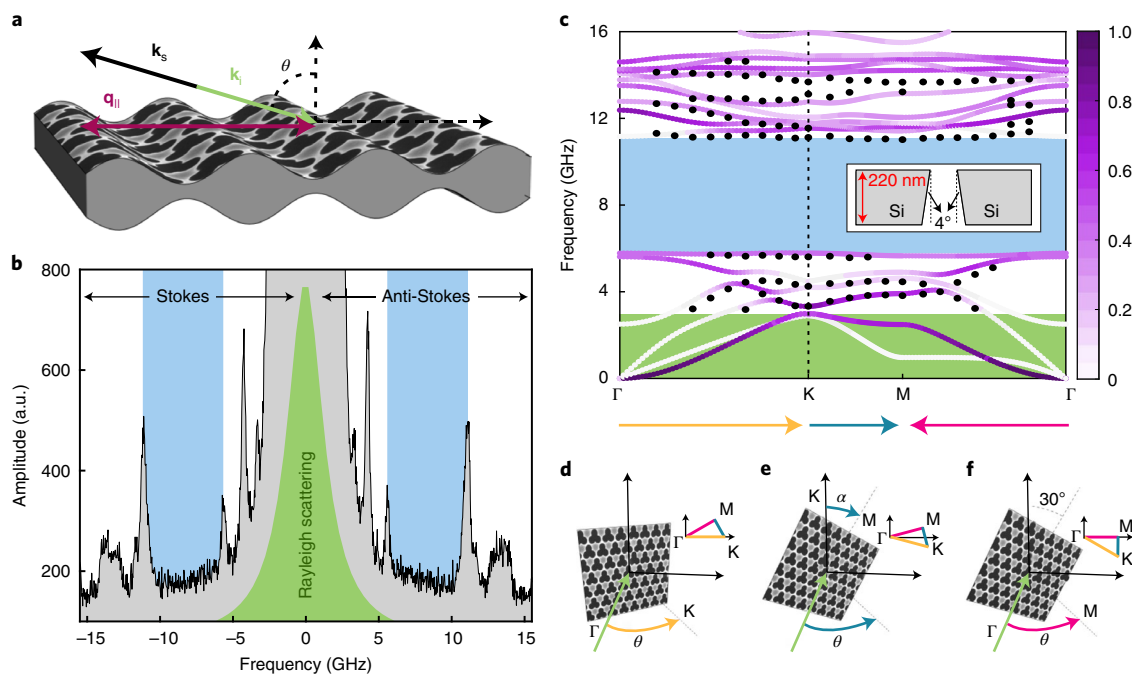
Fig. 2 | Brillouin light scattering spectroscopy. a, Schematic illustration of Brillouin scattering with the phase-matching condition for the backward configuration used in the experiments. Here, k_i and k_s represent the incident and the scattered light, respectively, and $q_\parallel$ is the parallel mechanic wavevector. The magnitude of $q_\parallel$ depends on the incident angle, where $q_\parallel = 2k_i \sin \theta$. **b**, Measured Brillouin scattering spectrum for an incident angle of $\theta = 32.5°$ with p-polarized light. The green central peak stems from elastic Rayleigh scattering. Negative and positive frequency peaks on either side of this large central peak correspond to Stokes and anti-Stokes contributions, respectively. The light-blue regions highlight the mechanical gap. **c**, Calculated dispersion relation based on the geometrical parameters obtained from SEM images of the fabricated samples that include a 4° sidewall angle correction in the vertical profile (inset). The black dots represent the measured frequencies of vibrational modes for different angles and the vertical dotted line indicates the frequencies obtained from the measured spectrum shown in **b**. The intensity colour scale represents the normalized coupling coefficients for the moving-boundary perturbation. **d–f**, The direction in which the sample is physically rotated to scan along the highest-symmetry directions ΓK (**d**), KM (**e**) and ΓM (**f**). The green arrows indicate the direction of the incident laser light while the other coloured arrows correspond to the rotation direction during measurements, which represent (and are colour-consistent with) the highest-symmetry direction indicated in **c**.

varied. The vertical dashed line indicates the position of frequencies obtained for the spectrum shown in Fig. 2b.

To resolve the full mechanical dispersion relation, we map the highest-symmetry directions of the Brillouin zone: ΓK, KM and ΓM. The ΓK path is measured by varying the angle of incidence θ from zero to 32.5°, as depicted in Fig. 2d where the green arrow represents the incident laser. Here, the value of the maximum angle θ is calculated from the relation $q_\parallel = |\Gamma K| = \frac{4\pi}{3a} = \frac{4\pi}{\lambda_i} \sin \theta$. To map the ΓM direction, we rotate the sample 30° to align the ΓM path with the horizontal direction as indicated in Fig. 2f and, from that position, we rotate the angle θ. Here, the maximum angle is indicated by $q_\parallel = |\Gamma M| = \frac{2\pi}{\sqrt{3}a} = \frac{4\pi}{\lambda_i} \sin \theta$. Mapping the KM path requires the simultaneous variation of two specific angles α and θ to measure the intersecting point of the blue segment and the horizontal direction, as depicted in Fig. 2e.

The calculated and measured frequencies are in good agreement and we attribute the residual frequency mismatch to fabrication fluctuations and the non-vertical sidewalls. Some modes in Fig. 2c are undetectable in the experiment as their displacement is predominantly in-plane and therefore do not scatter enough light to be detected. The light-blue region in Fig. 2c highlights the mechanical gap of this particular crystal. Within this frequency window, no elastic waves were measured for any angle of incidence in any high-symmetry direction, covering a broad spectral range of 5.3 GHz centred at 8.4 GHz, which corresponds to a gap-to-midgap ratio of 64%. We also explore the spectral tunability of the gap as a function of the geometry by varying the lattice constant a. The band-gap evolution calculated from finite-element simulations and

measured spectra for crystals with periods of 220 nm, 330 nm and 440 nm can be found in Supplementary Section 5. Supplementary Figure 11 also includes the experimental band reconstruction for crystals with $a = 220$ nm and $a = 440$ nm. We confirm the spectral tunability of the gap from 4 GHz to 11.5 GHz. Subsequently, the tuning of phononic guided modes is also possible.

Mapping of waveguide guided modes
Finally, we demonstrate the possibility to create phononic waveguides with the phononic insulator presented here. For this, we design and fabricate a waveguide surrounded on both sides by shamrock phononic crystals with inverted symmetry as shown in the SEM image in Fig. 3a. This structure has a periodicity of $a = 440$ nm, a waveguide width of $w = 184$ nm, and the same fill fraction and thickness as the previous structures ($r/a = 0.22$, $t = 220$ nm). The mirror symmetry of the crystal with respect to the defect line is crucial for proper band engineering of the guided elastic waves. The two panels in Fig. 3b show the Brillouin spectra measured on the waveguide (top) and on the surrounding phononic crystal (bottom), as specified in the insets, taken at the same incident angle of 23.8°. The blue region indicates the phononic band-gap of the structure. The two peaks measured within this gap in the top panel of Fig. 3b at 5.7 GHz and 7.1 GHz are clear experimental evidence of mechanical vibrations confined in the phononic waveguide.

In order to detect these confined modes, it is necessary to focus the light on the waveguide with a long-working distance microscope objective to reduce the spot size of the incident light down to 1.2 μm. In doing so, we reduce the contribution of the Brillouin
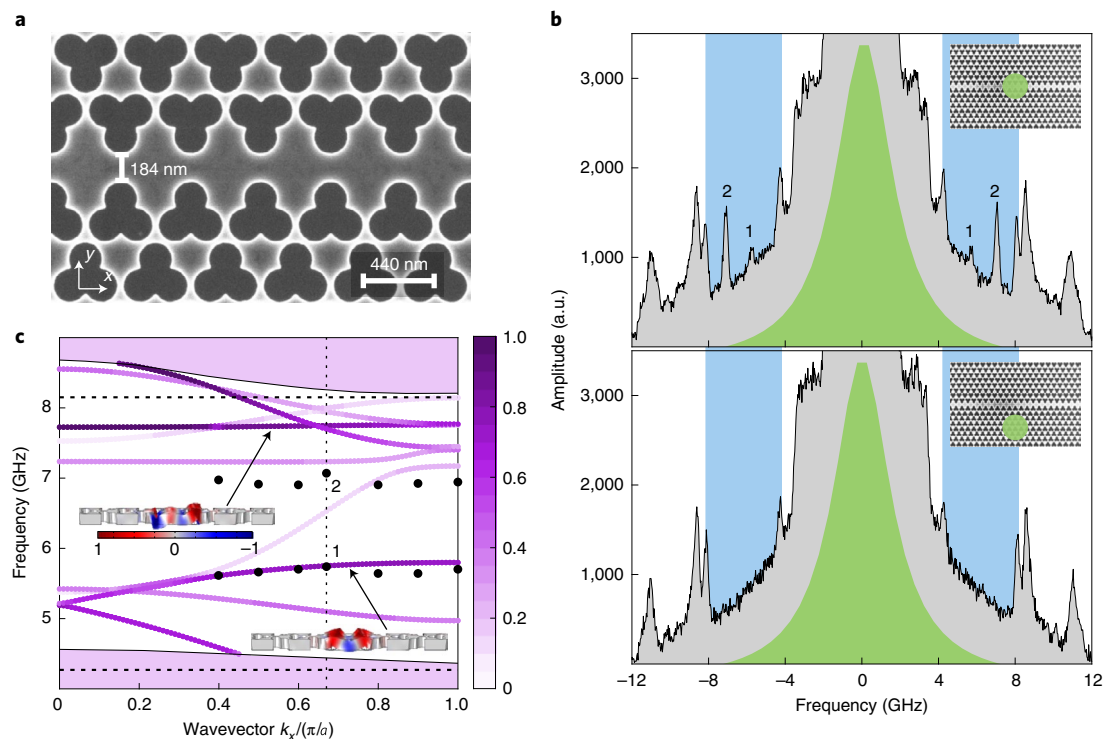
Fig. 3 | Hypersonic phononic waveguide. a, SEM image of a shamrock phononic waveguide with a lattice period of $a = 440$ nm and waveguide width of $w = 184$ nm. The thickness and radius of the structure are the same as in previous structures ($t = 220$ nm, $r = 0.22a$). **b**, Measured Brillouin scattering spectra in the waveguide (top) and surrounding phononic crystal (bottom) as is illustrated in the insets, for an incident light angle of 23.8°. The spectral width of the measured gap is indicated by the blue regions. Two peaks whose frequencies correspond with the guided modes of the system appear inside the gap in the spectrum of the waveguide (top). **c**, The calculated dispersion relation of the waveguide. The intensity colour scale represents the normalized coupling coefficient for the moving-boundary perturbation. The horizontal and vertical dotted lines indicate the mechanical band edges and phononic wavevector, respectively, while the black dots represent the frequencies of peaks 1 and 2, all for the top waveguide spectrum shown in **b**. Insets: the mode profiles for the indicated bands where the colour represents the normalized out-of-plane displacement.

scattered signal from the crystal while increasing the contribution from the waveguide. For the measurements of these waveguide structures, the background is higher due to a greater collection of reflected and linearly scattered light relative to that of the 3 cm focal length lens used in Fig. 2. Figure 3c plots the dispersion relation of the waveguide accounting for the 4° correction of the vertical sidewalls. As in Fig. 2c, the colour intensity of the bands corresponds to the normalized coupling coefficient for the moving-boundary perturbation. The fully shaded regions above and below the gap correspond to the bulk crystal modes and define the band-gap edges of the structure.

The calculated dispersion relation exhibits nine guided modes but only two (which are indicated with their associated mode profiles) are detected in our experiment. We attribute this to be because of the elastic displacement of these modes, which is predominantly out-of-the plane, while the other calculated guided modes displace the structure primarily in-plane (Supplementary Section 4). The horizontal dashed lines highlight the edges of the band-gap measured in Fig. 3b and the black dots correspond to the frequencies of the guided modes measured at different angles. The angle $\theta = 23.8°$ corresponds to a normalized wavevector of 1.34 (replacing $q_{\parallel} = n\pi/a$ in equation (1) and solving n), or $k_x/(\pi/a) = 0.66$ over the first periodic zone of the waveguide. The two black dots (1 and 2) coincide with the measured frequencies and wavevector in Fig. 3b. We assume that the measured peak around 7 GHz corresponds with the darker flat mode around 7.7 GHz and not with the lighter curve that it is spectrally closer to. There is a difference of approximately 700 MHz for this band while the other peaks agree very closely with the calculated band. The detection of these two modes

is a clear fingerprint of the existence of guided modes along the Shamrock waveguide.

Conclusions

In summary, we provide direct experimental evidence of the complete absence of mechanical vibrations at room temperature within a full phononic band-gap that is 5.3 GHz wide with a central frequency of 8.4 GHz. This measured mechanical gap has a gap-to-midgap ratio of 64% and is an order of magnitude wider than previous experimental demonstrations reported in the literature. The geometric pattern we incorporate gives rise to these wide mechanical gaps by distributing the mass within the unit cell, forming mass clusters connected by narrow necks that result in the destructive interference of phonon waves. We achieve control over the width and frequency of the gap by fine-tuning of the geometrical parameters of the structure, enabling spectral tunability of the gap from 4 GHz to 11.5 GHz. This tunability is extended to the guided modes of a line-defect waveguide, enabling engineering of the frequency and number of confined modes within the structure. This is a clear demonstration of mechanical guided modes at hypersonic frequencies in the gigahertz regime using line-defect waveguides, measured at room temperature without any external excitation in a SOI platform that enables facile integration into existing photonic systems. This hypersonic insulator is also a photonic insulator for transverse-electric modes at telecom wavelengths[26,27] and can be used to simultaneously engineer phononic and photonic transport enhancing the optomechanical coupling between terahertz photons and gigahertz phonons. This makes the crystal an ideal transducer in photonic circuits with potential applications

in high-speed signal processing[39]. Furthermore, this platform can be used in applications and physical processes in which a wide mechanical band-gap is required to isolate the system from thermal damping, such as in quantum cavity optomechanics or organic molecular systems[40].

Online content

Any methods, additional references, Nature Research reporting summaries, source data, extended data, supplementary information, acknowledgements, peer review information; details of author contributions and competing interests; and statements of data and code availability are available at https://doi.org/10.1038/s41565-022-01178-1.

References

1. Krause, A. G., Winger, M., Blasius, T. D., Lin, Q. & Painter, O. A high-resolution microchip optomechanical accelerometer. *Nat. Photon.* **6**, 768–772 (2012).
2. Chaste, J. et al. A nanomechanical mass sensor with yoctogram resolution. *Nat. Nanotechnol.* **7**, 301–304 (2012).
3. Gavartin, E., Verlot, P. & Kippenberg, T. J. A hybrid on-chip optomechanical transducer for ultrasensitive force measurements. *Nat. Nanotechnol.* **7**, 509–514 (2012).
4. Teufel, J. D. et al. Sideband cooling of micromechanical motion to the quantum ground state. *Nature* **475**, 359–363 (2011).
5. Chan, J. et al. Laser cooling of a nanomechanical oscillator into its quantum ground state. *Nature* **478**, 89–92 (2011).
6. Sigalas, M. & Economou, E. N. Band structure of elastic waves in two dimensional systems. *Solid State Commun.* **86**, 141–143 (1993).
7. Kushwaha, M. S., Halevi, P., Dobrzynski, L. & Djafari-Rouhani, B. Acoustic band structure of periodic elastic composites. *Phys. Rev. Lett.* **71**, 2022 (1993).
8. Martínez-Sala, R. et al. Sound attenuation by sculpture. *Nature* **378**, 241 (1995).
9. Gorishnyy, T., Ullal, C. K., Maldovan, M., Fytas, G. & Thomas, E. L. Hypersonic phononic crystals. *Phys. Rev. Lett.* **94**, 115501 (2005).
10. Zen, N., Puurtinen, T. A., Isotalo, T. J., Chaudhuri, S. & Maasilta, I. J. Engineering thermal conductance using a two-dimensional phononic crystal. *Nat. Commun.* **5**, 3435 (2014).
11. Eichenfield, M., Chan, J., Camacho, R. M., Vahala, K. J. & Painter, O. Optomechanical crystals. *Nature* **462**, 78–82 (2009).
12. Djafari-Rouhani, B., El-Jallal, S. & Pennec, Y. Phoxonic crystals and cavity optomechanics. *C. R. Phys.* **17**, 555–564 (2016).
13. MacCabe, G. S. et al. Nano-acoustic resonator with ultralong phonon lifetime. *Science* **370**, 840–843 (2020).
14. Fang, K., Matheny, M. H., Luan, X. & Painter, O. Optical transduction and routing of microwave phonons in cavity-optomechanical circuits. *Nat. Photon.* **10**, 489–496 (2016).
15. Patel, R. N. et al. Single mode phononic wire. *Phys. Rev. Lett.* **121**, 040501 (2018).
16. Ren, H. et al. Two-dimensional optomechanical crystal cavity with high quantum cooperativity. *Nat. Commun.* **11**, 3373 (2020).
17. Gomis-Bresco, J. et al. A one-dimensional optomechanical crystal with a complete phononic band gap. *Nat. Commun.* **5**, 4452 (2014).
18. Mohammadi, S., Eftekhar, A. A., Khelif, A., Hunt, W. D. & Adibi, A. Evidence of large high frequency complete phononic band gaps in silicon phononic crystal plates. *Appl. Phys. Lett.* **92**, 221905 (2008).
19. Soliman, Y. M. et al. Phononic crystals operating in the gigahertz range with extremely wide band gaps. *Appl. Phys. Lett.* **97**, 193502 (2010).
20. Gorisse, M. et al. Observation of band gaps in the gigahertz range and deaf bands in a hypersonic aluminum nitride phononic crystal slab. *Appl. Phys. Lett.* **98**, 234103 (2011).
21. Benchabane, S. et al. Guidance of surface waves in a micron-scale phononic crystal line-defect waveguide. *Appl. Phys. Lett.* **106**, 081903 (2015).
22. Otsuka, P. H. et al. Broadband evolution of phononic-crystal-waveguide eigenstates in real- and k-spaces. *Sci. Rep.* **3**, 3351 (2013).
23. Cheng, W., Wang, J., Jonas, U., Fytas, G. & Stefanou, N. Observation and tuning of hypersonic bandgaps in colloidal crystals. *Nat. Mater.* **5**, 830–836 (2006).
24. Graczykowski, B. et al. Phonon dispersion in hypersonic two-dimensional phononic crystal membranes. *Phys. Rev. B* **91**, 075414 (2015).
25. Liu, Q., Li, H. & Li, M. Electromechanical Brillouin scattering in integrated optomechanical waveguides. *Optica* **6**, 778–785 (2019).
26. Söllner, I., Midolo, L. & Lodahl, P. Deterministic single-phonon source triggered by a single photon. *Phys. Rev. Lett.* **116**, 234301 (2016).
27. Arregui, G., Navarro-Urrios, D., Kehagias, N., SotomayorTorres, C. M. & García, P. D. All-optical radio-frequency modulation of Anderson-localized modes. *Phys. Rev. B* **98**, 180202 (2018).
28. COMSOL Multiphysics v.5.1 (COSMOL Inc., 2022).
29. Safavi-Naeini, A. H. & Painter, O. Design of optomechanical cavities and waveguides on a simultaneous bandgap phononic-photonic crystal slab. *Opt. Express* **18**, 14926–14943 (2010).
30. Kargar, F. & Balandin, A. A. Advances in Brillouin–Mandelstam light-scattering spectroscopy. *Nat. Photon.* **15**, 720–731 (2021).
31. Carlotti, G. Elastic characterization of transparent and opaque films, multilayers and acoustic resonators by surface Brillouin scattering: a review. *Appl. Sci.* **8**, 124 (2018).
32. Boyd, R. W. *Nonlinear Optics* 3rd edn (Academic Press, 2008).
33. Johnson, S. G. et al. Perturbation theory for Maxwell's equations with shifting material boundaries. *Phys. Rev. E* **65**, 066611 (2002).
34. Van Laer, R., Kuyken, B., Van Thourhout, D. & Baets, R. Interaction between light and highly confined hypersound in a silicon photonic nanowire. *Nat. Photon.* **9**, 199–203 (2015).
35. Florez, O. et al. Brillouin scattering self-cancellation. *Nat. Commun.* **7**, 11759 (2016).
36. Cuffe, J. et al. Phonons in slow motion: dispersion relations in ultrathin Si membranes. *Nano Lett.* **12**, 3569–3573 (2012).
37. Brillouin, L. Diffusion de la lumière et des rayons X par un corps transparent homogène. *Ann. Phys.* **9**, 88–122 (1922).
38. Loudon, R. & Sandercock, J. R. Analysis of the light-scattering cross section for surface ripples on solids. *J. Phys. C* **13**, 2609 (1980).
39. Shin, H. et al. Control of coherent information via on-chip photonic-phononic emitter-receivers. *Nat. Commun.* **6**, 6427 (2015).
40. Gurlek, B., Sandoghdar, V. & Martin-Cano, D. Engineering long-lived vibrational states for an organic molecule. *Phys. Rev. Lett.* **127**, 123603 (2021).

Methods

Methods are available in the Supplementary Information.

Data availability

Data supporting the results and conclusions are available at https://doi.org/10.5281/zenodo.6610862.

Author contributions

O.F. designed, simulated and characterized the samples. M.A. and S.S. fabricated the samples. G.A., R.C.N. and J.G.-B. contributed to the data analysis. C.M.S.-T. and P.D.G. supervised the work. P.D.G. conceived the idea and the project. O.F. and P.D.G. wrote the manuscript with contributions and input from all authors.

Competing interests

The authors declare no competing interests.

Additional information

Supplementary information The online version contains supplementary material available at https://doi.org/10.1038/s41565-022-01178-1.

Correspondence and requests for materials should be addressed to O. Florez or P. D. García.

Peer review information *Nature Nanotechnology* thanks Ilari Maasilta and the other, anonymous, reviewer(s) for their contribution to the peer review of this work.

Reprints and permissions information is available at www.nature.com/reprints.